Cyclist Reynolds number effects and drag crisis distribution

Terra, W.; Sciacchitano, A.; Scarano, F.

DOI
10.1016/j.jweia.2020.104143

Publication date
2020

Document Version
Final published version

Published in
Journal of Wind Engineering and Industrial Aerodynamics

Journal of Wind Engineering & Industrial Aerodynamics 200 (2020) 104143

Contents lists available at ScienceDirect

Journal of Wind Engineering & Industrial Aerodynamics

journal homepage: www.elsevier.com/locate/jweia

Cyclist Reynolds number effects and drag crisis distribution

W. Terra *, A. Sciacchitano, F. Scarano

Aerospace Engineering Department, TU Delft, Netherlands

ARTICLE INFO

Keywords:
Cycling aerodynamics
Drag crisis
Reynolds number
Wind tunnel testing
Particle image velocimetry

ABSTRACT

The Reynolds number effects on body limbs of a cyclist model, namely leg and arm, are investigated via robotic volumetric Particle Image Velocimetry measurements in the velocity range from 5 m/s to 25 m/s. The near wakes of such body limbs feature recirculation regions whose width and length are governed not only by the taper of the body parts, but also by the presence of coherent streamwise vortical structures. Moreover, the interaction with the wakes of the upstream body parts plays a role in the local wake properties. While reductions of the wake width are observed on both lower leg and arm with increasing free-stream velocity, the wake of the upper leg follows an opposite trend increasing in size at higher velocity. Such variations of wake width with the Reynolds number are related to the behaviour of the local drag coefficient, indicating a drag crisis behaviour on both leg and arm. The distribution of the so-called *critical velocity* upon these body segments is discussed, as it determines the freestream speed where a minimum value for the drag can occur.

1. Introduction

In the last decade, cycling aerodynamics has become the subject of many scientific investigations aiming at a better understanding of the flow behaviour around the rider to identify specific sources of aerodynamic drag. The cyclist is typically modelled as a single bluff body or combination thereof. As such, the near-wake flow field features unsteady (Griffith et al., 2014; Crouch et al., 2016) and three-dimensional behaviour (Crouch et al., 2014; Jux et al., 2018). The flow topology is found to be dependent upon the rider's position (Defraeye et al., 2010) and the used equipment to a lesser extent (Chabroux et al., 2010 among others). Most prominent features of the wake flow are the pairs of counter-rotating thigh vortices that vary their position and strength during the pedalling cycle. The latter vortices are considered the cause of significant variations in the aerodynamic drag (Crouch et al., 2014; Griffith et al., 2014). Detailed knowledge of the flow around a cyclist is still needed when pursuing a systematic approach for the reduction of the aerodynamic drag, potentially increasing riding speed and overall performance. Reductions of the wind resistance have been achieved, among others, through modification of the bike frame and its components (Lukes et al., 2005), optimization of apparel (Brownlie et al., 2009) and posture (Defraeye et al., 2010; Blocken et al., 2018a), optimization of the interaction effects within small groups of riders (Barry et al., 2015), utilizing the surrounding conditions (Blocken et al., 2016) and individual positioning in a peloton (Blocken et al., 2018b).

Optimization of the athlete's apparel has received much attention in cycling as well as in other speed sports (skiing and skating; Oggiano, 2010). Reduction of cyclist aerodynamic drag has been proposed through manipulation of skinsuit surfaces on, among others, the cyclist's arms and legs (Brownlie et al., 2009). The main principle relies on the assumption that the flow around these body segments shows similarities with that of cylinders and spheres. As thoroughly discussed in the seminal papers of Achenbach (1968, 1972), flow separation around a convex geometry is dependent upon the Reynolds number, determining the regimes associated to laminar and turbulent separation. At low, sub-critical Reynolds numbers ($Re < 100{,}000$), the boundary layer on the surface of a smooth model remains laminar until it separates before the shoulder region of the model ($\Theta_s \sim 80°$, see Fig. 1), resulting in a wide wake and a relatively high drag coefficient (cylinders: $C_{D,sub} \sim 1.2$; spheres $C_{D,sub} \sim 0.4$). In the critical Reynolds number regime ($100{,}000 < Re < 500{,}000$), the separated shear layer undergoes transition to turbulence and reattaches onto the model surface with a significant downstream shift of the final separation ($\Theta_s \sim 130°$), thus yielding a reduced drag coefficient ($C_{D,crit} < 0.25C_{D,sub}$). This phenomenon is typically referred to as the *drag crisis* (e.g. Constantinescu and Squires, 2004; Lehmkuhl et al., 2014). The critical Reynolds number Re_{crit} is typically defined as the value obtained at the endpoint of the critical regime, where the drag coefficient reaches its minimum (Roshko, 1961; Schewe, 1983). Further increasing the

The data presented in the figures in this work is available online (http://doi.org/10.4121/uuid:6c704207-823e-4759-83df-473a57f5f5e9)

* Corresponding author.
E-mail address: w.terra@tudelft.nl (W. Terra).

https://doi.org/10.1016/j.jweia.2020.104143
Received 6 November 2019; Received in revised form 19 February 2020; Accepted 6 March 2020
Available online xxxx

Reynolds number into the super-critical regime, the boundary layer undergoes transition before separation, which increases again the drag coefficient.

This behaviour can be exploited to force the drag crisis at lower values, equal to the rider cycling velocity, when the body parts are dressed in textiles with specific surface roughness (e.g. Brownlie et al., 2009; Oggiano et al., 2009). The effect of tailored textile roughness is to enhance turbulent mixing in the surface boundary layer and delay its separation, thus achieving a drag crisis at lower speed (viz. Reynolds number; Achenbach, 1971; Achenbach and Heinecke, 1981). Surface properties manipulation may result into the ideal situation where critical flow conditions are encountered across all parts of the cyclist body.

The most practiced approach to evaluate the effectiveness for drag reduction of these dedicated textile designs consists of force balance measurements on two-dimensional cylinders. Given the geometrical complexity of the athlete's body and equipment, modelling the drag crisis only based on the hypothesis of circular or elliptical cylinders and superposition of effects may be considered a crude approach. In comparison to approximating cylinders, the cyclist flow and drag crisis behaviour is expected to be distorted by wake interactions (Okajima, 1977), junction regions (e.g. around elbow and knee; Park and Lee, 2000) and other three-dimensional features. Although, drag crisis behaviour is known to vary among individual body segments (Defraeye et al., 2011; D'Auteuil et al., 2012), variations along body segments have not been presented and the responsible flow Reynolds number effects are not yet understood. Hence, a detailed analysis of the three-dimensional flow topology and wake is of importance to understand how the drag crisis phenomenon occurs along the distributed surface of the cyclist.

The present study investigates the flow around body segments of a full-scale cyclist model in time trial position riding at different speeds employing robotic volumetric Particle Image Velocimetry (PIV). The experiment aims at characterizing Reynolds number effects along the cyclist's body and understand the circumstances for the drag crisis to occur. The static cyclist mannequin is a high-fidelity reproduction of the athlete shape, with legs in asymmetric position (one fully stretched and the other flexed). The attention of the present work focuses on the stretched leg, which produces more drag (Griffith et al., 2014) and where bluff body Reynolds number effects are expected more pronounced in comparison to the flexed leg. The position of the two arms is rather symmetrical to the cyclist's median plane, and the left arm is chosen for the investigation. To understand the highly complex cyclist flow, a general near-wake flow description at typical time trial speed is provided first, before the flow Reynolds number effects are discussed. The critical flow condition, corresponding to minimal drag coefficient, is inferred from the local wake width and its distribution along the arm and leg is finally presented so to understand what governs the cyclist drag crisis and how the drag of the cyclist may be minimized by dedicated skinsuits designs in the future.

2. Methodology

To assess the existence of the drag crisis on individual sections of the cyclist's body, the local drag coefficient of those sections must be evaluated. In this work, the local C_D of individual body parts is related to the near-wake flow properties. Roshko (1955) suggested the use of the wake width to characterize the bluffness of an object. In a later work (Roshko, 1961) a model was advanced, where the drag coefficient is directly proportional to the normalised wake width d_w/d (d being the object width) and the base pressure C_{pb}:

$$C_D = -C_{pb}\frac{d_w}{d} \tag{1}$$

However, the model described by equation (1) has shown good agreement with experimental data only in the sub-critical flow regime (Roshko, 1961). In the critical regime, instead, the change of the drag coefficient can be expressed in terms of the change in wake width (Rodriguez et al., 2015):

$$\frac{C_{D,1}}{C_{D,2}} = \alpha_d \frac{d_{w,1}}{d_{w,2}} \tag{2}$$

where $\alpha_d \sim 2$ is an empirical constant and the subscripts 1 and 2 refer to conditions of two different Reynolds numbers in the critical regime. Fig. 1 illustrates the change in drag coefficient and wake width between sub-critical and the critical condition. Based on the available literature, the relation between the drag coefficient and the wake width cannot be considered valid for quantitative analysis. It is generally used, however, to draw qualitative conclusions when large variations in the local drag coefficient are associated with variations of the Reynolds number.

In the present work, the wake width inferred from experiments is inspected over a range of freestream velocity to detect the occurrence of drag crisis. The critical flow condition is associated to a specific velocity, the critical velocity V_{crit}, instead of critical Reynolds number Re_{crit}. This choice enables a direct assessment of whether the different body parts of the cyclist racing at typical time-trial speed operate in the sub-critical, critical, or the super-critical flow regime.

3. Experimental setup and measurement procedures

3.1. Wind tunnel apparatus and cyclist mannequin

The experiments are conducted in the atmospheric closed-circuit Open Jet Facility (OJF) wind tunnel of the Aerospace Engineering Laboratories of the Delft University of Technology. The OJF features an area contraction ratio of 3:1 and jet exit cross section of 2.85 × 2.85 m^2. The OJF can operate at freestream velocity ranging from 4 to 35 m/s. The free-stream turbulence intensity is reported to be below 1% (Lignarolo et al., 2014). A full-scale cyclist mannequin is used in the experiments. The wind tunnel model is an in-house additive manufactured rigid body replica of an elite cyclist (Van Tubergen et al., 2017). The cyclist holds a position typical of time-trial events and is installed accordingly on a typical time-trial bike setup. The latter consists of a *Giant* Trinity Advanced Pro bike frame (size M) equipped with a Pro 3-spoke *Textreme* front and Pro disc *Textreme* rear wheel with 25 mm tubular tires (see Fig. 2). Steel rigid struts support the bike at the front and rear axis and connect it to the 6-component balance system. Except for a *Giro* Rivett TT helmet, the model is not wearing garments. In the present work, the natural drag crisis is investigated, in the absence of surface roughness

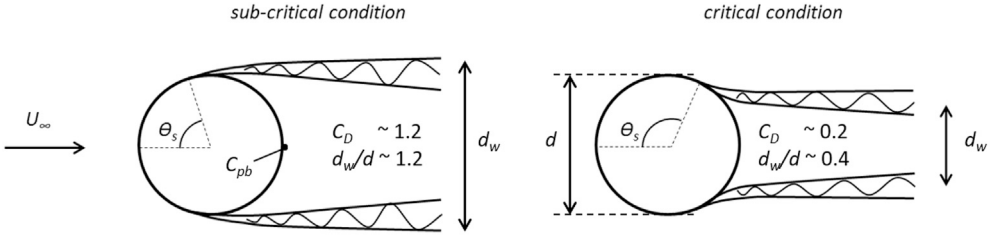

Fig. 1. Sketch of separated shear layers and wake width in sub-critical (left) and critical condition (right).

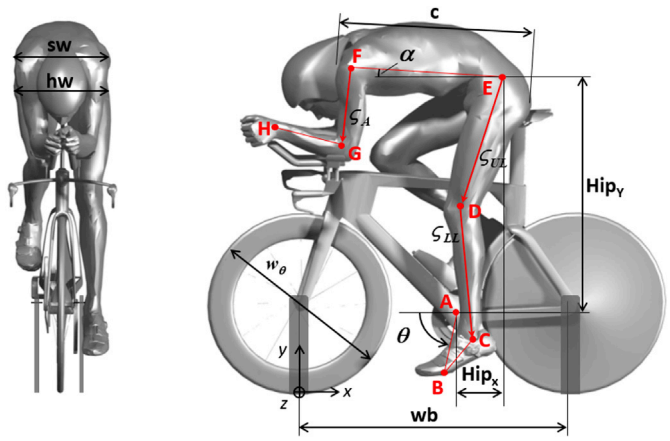

Fig. 2. Geometry of the cyclist mannequin with indication of reference system.

control. A mannequin surface roughness $k < 0.1$ mm is estimated after surface polishing treatment. To avoid model vibration during the measurements, which would otherwise occur above $U_\infty \sim 16$ m/s, four steel wires of 2 mm diameter connect the bike frame to the floor (Fig. 4-right). A flat plate is installed at the jet exit, elevated 40 cm from the wind tunnel contraction exit, to reduce the effect of boundary layer formation prior to the cyclist.

Although the rider's aerodynamic drag is reported to vary during pedalling (Crouch et al., 2014), in the current work the configuration with largest difference in leg position is examined, namely with the left leg completely stretched and the right one flexed. As a result, the model exhibits an asymmetric position with respect to the median *x-y* plane. This position relates to a $\Theta = 75°$ crank angle, with $\Theta = 0°$ being the configuration with horizontal crank arm and left foot forward. The main characteristics of the bike and cyclist mannequin are depicted in Fig. 2-right. The positions and lengths of the main segments are listed in Table 1.

The critical Reynolds number distribution is, among others, affected by the changing cross-sectional area shape and inclination of the body part axis. These geometrical features are illustrated in Fig. 3 reporting different cross-sections of the arm and stretched leg. As the leg narrows from the hip towards the foot, also the 'bluffness' of the leg changes. Especially closer to the foot ($y = 275$ mm; black cross-section), the aspect ratio d/l of the leg's cross-section decreases in comparison to the knee and upper leg from approximately 0.65 to 0.85, respectively. Changes in cross-sectional shape of the arm are accounted as well.

To allow a non-dimensional analysis of the cyclist's near-wake flow, a human body coordinate ζ is introduced that follows the cyclist limbs, namely the upper arm ζ_A ($\overline{FG}$: elbow to shoulder joint), the upper leg ζ_{UL} ($\overline{DE}$: hip to knee joint) and the lower leg ζ_{LL} ($\overline{CD}$: knee to ankle joint, see Fig. 2-right). The origin ($x_\zeta = 0$; $z_\zeta = 0$) of the body sections depicted in Fig. 3 is chosen at the intersection of the line segments connecting the different limbs joints and the different horizontal *y*-planes.

Table 1
Mannequin and bike characteristic lengths and angles.

Name	Symbol	Position/length
Crank angle	Θ	75°
Torso angle of attack	α	5°
Hip width	*hw*	365 mm
Shoulder width	*sw*	380 mm
Hip location x	Hip_x	180 mm
Hip location y	Hip_y	850 mm
Wheel base	*wb*	1003 mm
Wheel diameter	w_Θ	700 mm
Crank length	$\overline{AB}$	175 mm
Lower leg length	$\overline{CD}$	475 mm
Upper leg length	$\overline{DE}$	460 mm
Torso length	*c*	700 mm

3.2. Measurement apparatus and data analysis

Considering the three-dimensional complexity of the rider-bike geometry and the large-size of the measurement domain, a robotic Particle Image Velocimetry (Jux et al., 2018) system is employed. The robotic PIV technique combines coaxial volumetric velocimetry (CVV, Schneiders et al., 2018) and neutrally buoyant sub-millimeter helium-filled soap bubbles (HFSB) as tracers for large-scale aerodynamic measurements in wind tunnels (Scarano et al., 2015; Caridi et al., 2016). A seeding system operates 200 HFSB generators over a cross section of 1 (H) × 0.5 (W) m^2. Fig. 4 depicts the system installed in the settling chamber of the OJF. The seeded streamtube in the test section upstream of the cyclist is approximately 60 × 30 cm^2. The seeding array is translated vertically to cover the whole cross section of the rider. The average tracer concentration during experiments varies from 0.2 to 1 bubbles/cm^3 depending on the freestream velocity (Caridi et al., 2016). The presence of the seeding system upstream is reported to increases the freestream turbulence intensity from 0.5% to approximately 0.8% (Giaquinta, 2018).

The CVV system features four CMOS cameras arranged in a compact holder. The CVV probe is installed on a 6-degree-of-freedom Universal Robots A.S. *UR5* robotic arm that translates and rotates the optical head (see Fig. 4) with a positional repeatability of ±0.03 mm and ±0.01°, respectively. Aerodynamic interference effects from the robotic PIV system are within 2% (Giaquinta, 2018).

A Quantronix *Darwin Duo* Nd:YLF laser (25 mJ pulse energy at 1 kHz) is directed, into an optical fibre and transmitted towards the LaVision GmbH *Minishaker Aero* CVV probe. The measurement volume features a conical shape with cross-sections of approximately 10 cm and 40 cm diameter at 20 cm and 60 cm from the probe, respectively. The main specifications of the system are summarized in Table 2.

To cover the relevant range of Reynolds number where the drag crisis is expected to occur, the measurements are conducted within the velocity range U_∞ = [5 10 15 20 25] m/s. The corresponding Reynolds number ranges from 2.3 × 10^5 to 1.2 × 10^6 based on the torso chord ($c = 700$ mm; Fig. 2).

A geometrical calibration of the system is performed following Jux et al. (2018). The time-average velocity and the velocity fluctuations are obtained adopting the multi-Δt 3D-PTV approach (Saredi et al., 2019) using the Shake-the-Box (STB, Schanz et al., 2016) double-frame algorithm in *Davis 10* from Lavision GmbH. The pulse separations of the initial measurement, used as predictor, Δt_1 is chosen to yield a tracer displacement of approximately 3 mm in the freestream. The measurement dynamic velocity range (Adrian, 1997) of the measurement is enlarged with a second acquisition of image pairs separated by Δt_2 corresponding to 10 mm displacement in the freestream. At each position of the CVV, a total of 2000 and 6000 image pairs are collected at Δt_1 and Δt_2, respectively, at a rate of 300 Hz, to produce statistically converged velocity estimates. The measurements are conducted scanning through 25 different probe positions for each setting of the freestream velocity, resulting in a total of 250 data sets.

3.3. Image pre-processing and data reduction

The background noise and reflections in the acquired PIV images are mitigated applying, a Gaussian smoothing in space (kernel size of 5 × 5 pixels) and a high-pass frequency filter (Sciacchitano and Scarano, 2014). The flow velocity information is then retrieved via Lagrangian Particle Tracking (Shake-the-Box algorithm, Schanz et al., 2016, in the LaVision *DaVis 10* software). Velocity statistics are obtained from the Lagrangian velocity ensemble, combining all CVV probe positions, within cubic bins of 3 × 3 × 3 cm^3 with 75% overlap (Agüera et al., 2016) requiring at least 20 particles per bin.

The wake width is estimated from the obtained velocity statistics as the distance between the two shear layers. Fig. 5 depicts the non-dimensional time-average streamwise velocity, $\overline{u}/U_\infty$(left) obtained in the near-wake of the knee at $y = 650$ mm and $x_\zeta/d = 0.8$, d being the

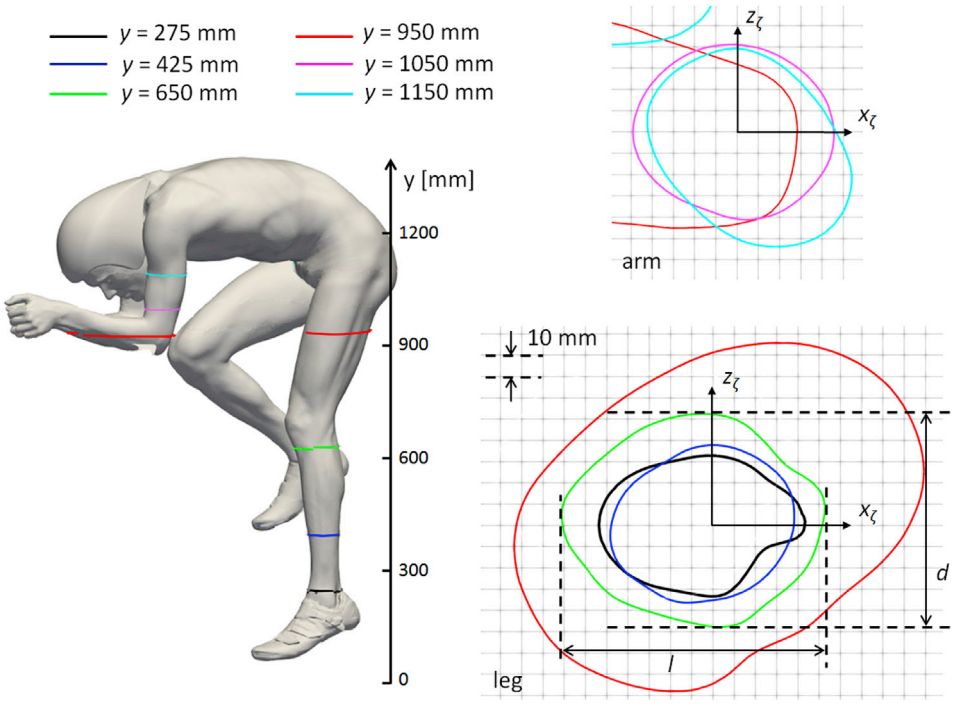

Fig. 3. Three-dimensional view of the cyclist mannequin with positions of considered cross sections (left). Contours of cross-sections (right).

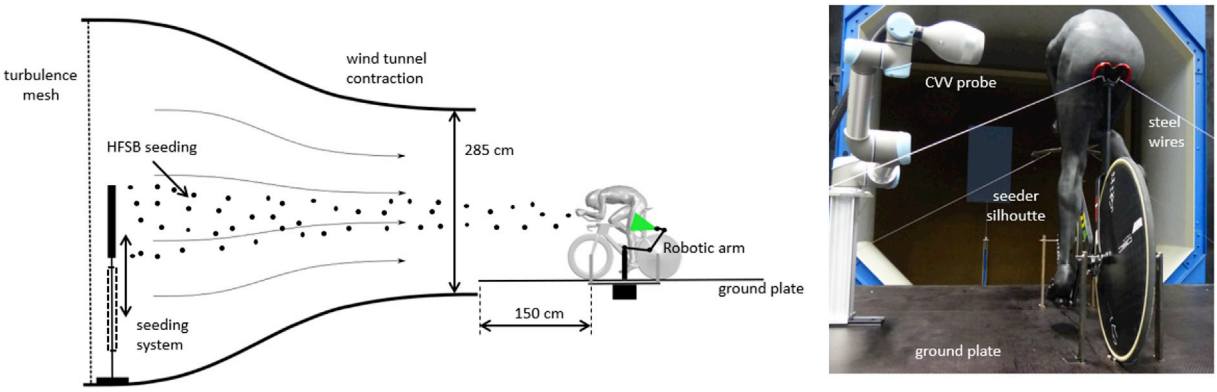

Fig. 4. Wind tunnel experimental setup: A schematic view (left) and a photo (right) depicting the robotic volumetric PIV components.

Table 2
Coaxial Volumetric Velocimeter specifications.

Optics	Focal length	4 mm
	Cameras numerical aperture	11
Imaging	Tomographic aperture (horizontal, vertical)	4°, 8°
	Sensor size	640 × 475 px^2
	Pixel pitch	4.8 μm
	Maximum acquisition frequency	758 Hz
	Bit depth	10
Illumination	Nominal pulse energy	25 mJ
	Wavelength	527 nm

width of the cyclist's leg at the given height y. Norberg (1983) suggested to evaluate the wake width from the distance between the velocity fluctuations peaks in the shear layers (Fig. 5-middle). However, velocity fluctuations are less accurately captured with the CVV technique (Schneiders et al., 2018). The location of peak velocity fluctuations is known to coincide with the velocity inflection points (e.g. White and Nepf, 2008; Unnikrishnan and Gaitonde, 2019) and, hence, the wake width is instead evaluated as the distance between the velocity inflection points, i.e. the distance between the peaks of $|\partial\overline{u}/\partial z|$ (Fig. 5-right). The wake width is estimated at $x_\zeta/d = 0.8$, d being the width of the cyclist's leg at the given height y. The latter choice comes as a trade-off between the need to avoid the measurement noise stemming from reflections close to the model and the detectability of $\partial\overline{u}/\partial z$ peak position with increasing distance from the model.

The position of the left and right shear layer is measured along the y-direction. The variations along y are regularized using a moving average filter (kernel size of 5 points, 37.5 mm) that reduces measurement uncertainties.

3.4. Experimental uncertainty

The uncertainty of the time-average velocity stems mainly from the unsteadiness of the cyclist's wake and from the random errors in the CVV measurements. The relative random uncertainty at 95% confidence level is evaluated as $\varepsilon_{\overline{u}} = k\sigma_u/(U_\infty\sqrt{N_p})$, σ_u being the standard deviation of the measured streamwise velocity, N_p the number of tracer particles per bin and $k = 1.96$ the coverage factor. In the freestream ($N_p \sim 5000$; $\sigma_u/U_\infty \sim 0.07$) and near-wake ($N_p \sim 500$; $\sigma_u/U_\infty \sim 0.5$ in the shear layers),

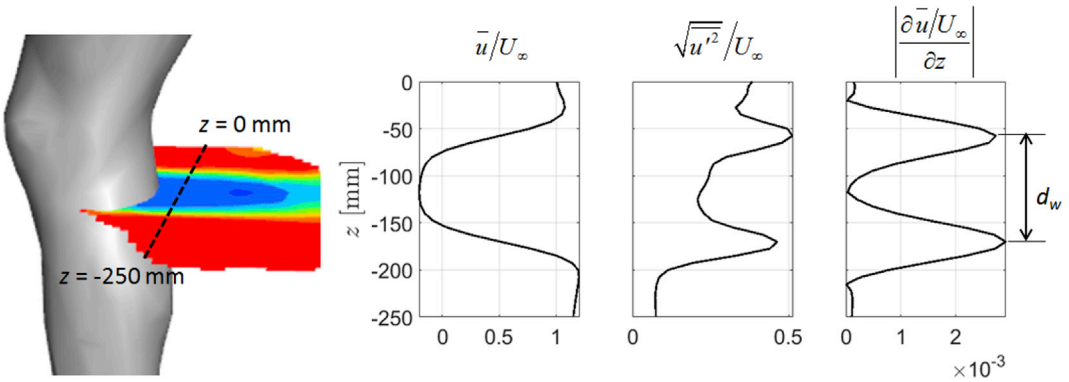

Fig. 5. Wake width estimation: Profiles of streamwise velocity (left), velocity fluctuations (middle) and spanwise velocity gradient (right).

the uncertainty values are approximately 0.2% and 4.5%, respectively. The uncertainty of the wake width evaluation is estimated as $\varepsilon_{dw} = \sqrt{2}\,h$ ~10 mm, being h = 7.5 mm the spacing between adjacent velocity vectors. Furthermore, the uncertainty of the critical velocity,$\varepsilon_{V,crit}$ is defined as the velocity range in which $|d_{w,Vcrit} - d_{w,v}| < \varepsilon_{dw}$, $d_{w,Vcrit}$ being the wake width at the critical velocity and $d_{w,V}$ the wake width at neighbouring freestream speeds. In addition, a minimum uncertainty of the critical velocity corresponds to the resolution of the selected increase in freestream velocity: $\varepsilon_{V,crit}$ = 2.5 m/s.

Finally, note that the effect of blockage (4% model blockage) is assumed negligible, considering the small estimated velocity correction for an open-jet wind tunnel (~1.01U_∞; Terra et al., 2019) in comparison to the freestream velocity resolution.

4. Results

4.1. Global flow structure and topology

The main features of the flow around the cyclist are surveyed at free stream velocity U_∞ = 15 m/s, typical of race conditions. Fig. 6 depicts contours of the time-average streamwise velocity (left), vertical velocity (middle) and streamwise velocity fluctuations (right) over multiple horizontal and vertical planes. Recirculation regions are identified by iso-surfaces of null streamwise velocity in the wake of the leg, upper arm and hip. The arm's recirculation region is relatively wide at the junction to the trunk as a consequence of interference with the head wake (marked in Fig. 6-top-left). The recirculation region narrows from the arm-trunk junction towards the elbow and disappears at the junction of lower and upper arm. The latter is firstly ascribed to a turbulent separation on the elbow as a consequence of the presence of the upstream lower arm. Secondly, the upwash of air resulting from the triplet of streamwise vortices emanating from the elbow (Fig. 7-left) injects high momentum fluid into the arm's wake and displaces the separation to the upper region of the arm. The latter resembles the flow topology across the free end of a cylinder in cross flow (e.g. Kawamura et al., 1984; Park and Lee, 2000).

Along the leg, from ankle to trunk, the width and downstream extension of the recirculation region increases, partly due to the thickening of the leg. It is remarkable, though, that the geometry of the recirculation region is not directly proportional to the local thickness of the body limbs: for example, the extension of the recirculation region at the lower thigh is approximately 45% of that at the knee (marked L_{LT} and L_k in Fig. 6, respectively), while the local thickness of the leg only decreases by approximately 10%. This reduction stems instead from the action of a counter rotating vortex pair that injects high speed fluid from

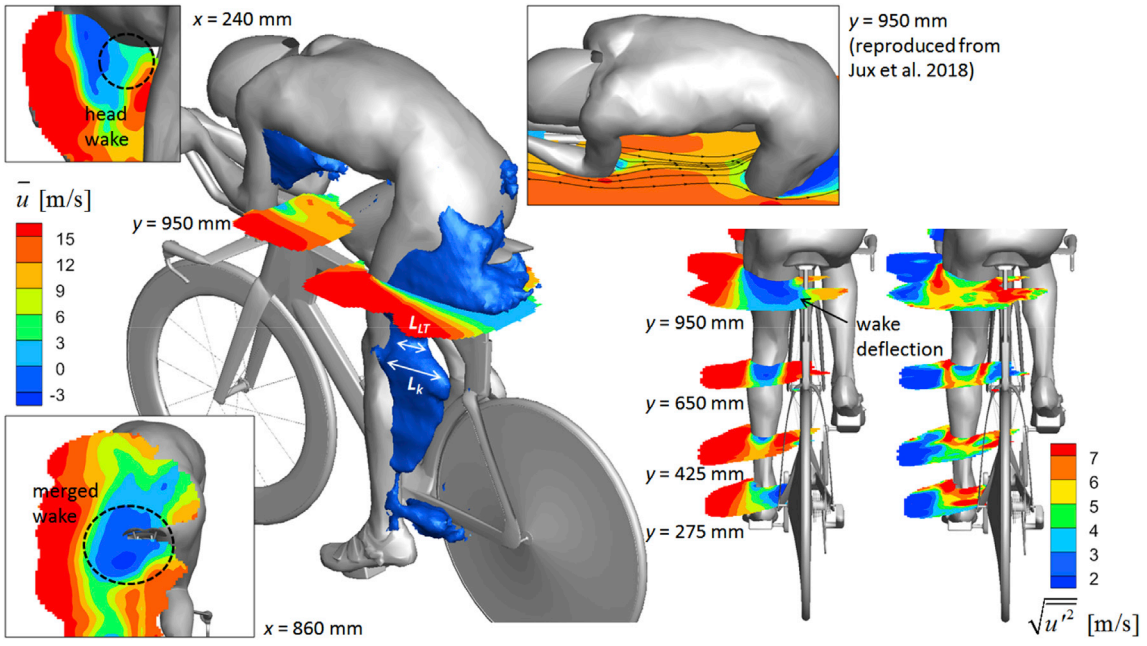

Fig. 6. Contours of time-average streamwise velocity (all subfigures except that on the right), streamwise velocity fluctuations (right subfigure) and an iso-surface of zero streamwise velocity.

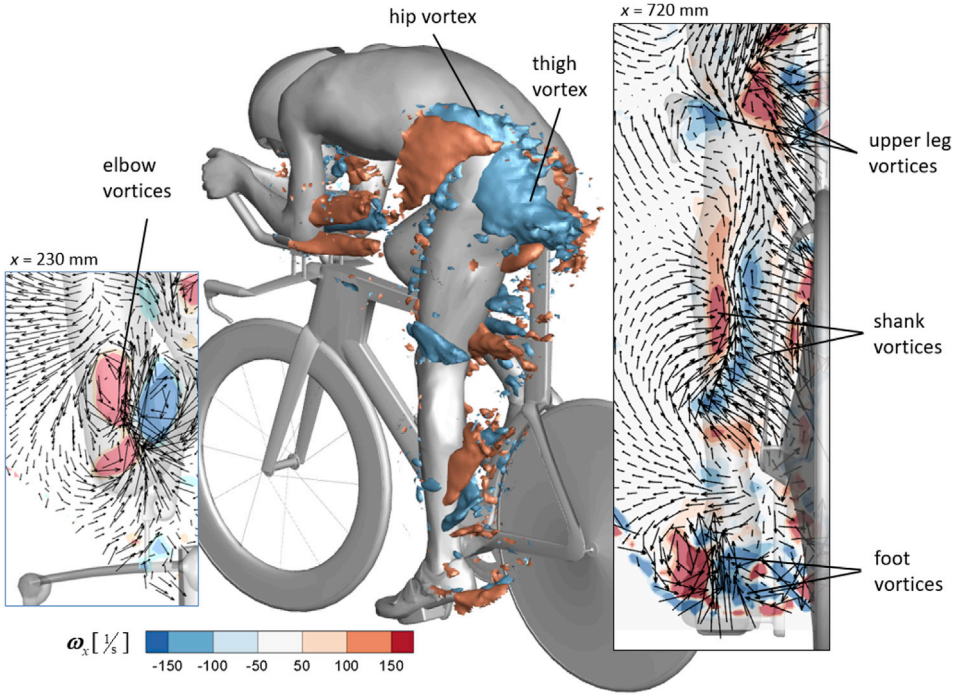

Fig. 7. Time-average streamwise vorticity (contours and iso-surfaces at −120 and 120 rad/s in blue and red, respectively) and in-plane vectors downstream of the upper arm and the leg (left and right, respectively). (For interpretation of the references to colour in this figure legend, the reader is referred to the Web version of this article.)

the upper leg (indicated in Fig. 7-right). As a result, the streamwise velocity downstream of the knee is increased and separation delayed. Similarly, the shank vortices are responsible for the suppression of the recirculation region towards the ankle. Despite the wake of the ankle being governed by streamwise vortex pairs, a small recirculation is expected in that region. The measurements do not capture it, likely due to its shallow form and the limited spatial resolution. The recirculation region is widest close to the junction of the legs (see Fig. 6-right; $y = 950$ mm), partly resulting from the leg tapered geometry. Additionally, the wakes of the left and right leg merge at $y > 900$ mm (indicated Fig. 6-bottom left), somehow similarly to that of two closely spaced side-by-side cylinders (Zdravkovich, 1987), which further increase the wake width. The observed deflection of the wake (indicated in Fig. 6-right) is also ascribed to the merged wakes.

The lower section of the leg (Fig. 6-right; $y = 425$ mm and $y = 650$ mm) exhibits a flow behaviour more closely resembling that of a two dimensional bluff body: two shear layers emanate from the sides of the leg, bounding a region of flow recirculation region. Outside of the shear layers, the flow velocity is close to the free-stream value. Closer to the junction of the two legs (Fig. 6-right; $y = 950$ mm), the inner shear is not clearly observed anymore and, instead, a wide turbulent region is present downstream of the seat post, which may be ascribed to a turbulent leg's approach flow stemming from the upstream arm (discussed in next paragraph). The flow across the foot is characterized by a pair of counter-rotating streamwise vortices (Fig. 7-right) and an interaction with the flow across the rear wheel and the bike's left crank, resulting in a sidewise deflection of the recirculation region towards the bike (Fig. 6-right; $y = 275$ mm). Finally, the main counter-rotating vortex pair originating from the hips and thighs and well documented in the literature (e.g. Crouch et al., 2014; Jux et al., 2018), are observed here too (marked in Fig. 7-middle).

The present measurement domain excludes the area downstream of the arm and upstream of leg between 420 mm $< x <$ 580 mm. To understand the interaction between the flow across the arm and leg, the data collected by Jux et al. (2018) is used to depict streamlines between the two (Fig. 6-top-right). It is observed that the outside of the left upper leg is mostly exposed to undisturbed flow, while the flow across the inside of the upper leg is largely governed by disturbed flow emanating from the arm.

Finally, it is noted that the wakes emanating from the steel wires have not been observed in the time-average flow field and, hence, their effect on the present results is assumed negligible. This is attributed to the relatively small size of the wires and the corresponding wakes in comparison to the size of the spatial bins used to average the Larangian velocity.

4.2. Reynolds number effects across individual body parts

4.2.1. The cyclist's stretched leg

Fig. 8 depicts contours of dimensionless streamwise velocity $\overline{u}/U_\infty$ in the horizontal planes $y = 950$ mm (top) and $y = 650$ mm (middle) and iso-surfaces of $\overline{u}/U_\infty = 0.2$ (bottom). From the latter it is observed that the wake of the lower leg and the knee generally narrows and shortens between $U_\infty = 5$ m/s and 20–25 m/s. More, specifically the length of the recirculation region, L/d, at $y = 650$ mm (Fig. 8-middle) decreases monotonically by about 25% from approximately $L/d = 2.2$ to $L/d = 1.7$, respectively (see also Table 3). Similarly, also the peak reverse flow velocity $\left|\overline{u_{\min}}\right|$ decreases by 25% from −0.24 to −0.18. Closer to the foot, at $y = 425$ mm, the recirculation length decays by approximately 35% between $U_\infty = 5$ m/s and 25 m/s. These trends are similar to those reported for spherical flow between sub-critical and critical conditions (Constantinescu and Squires, 2004; Tenada, 1978), suggesting that the critical condition at the knee and the lower leg occur approximately at 20 m/s and 25 m/s, respectively. The reported Reynolds number effects for cylinder flow in the critical regime, instead, are partly opposite, with an increasing length of the recirculation region throughout the critical regime (Rodriguez et al., 2015). The better similarity to the flow around a sphere may be related to the presence of the streamwise vortices dominating the wake of the leg, whereas similar vortical structures characterize instantaneous spherical flow topology (e.g. Constantinescu and Squires, 2004).

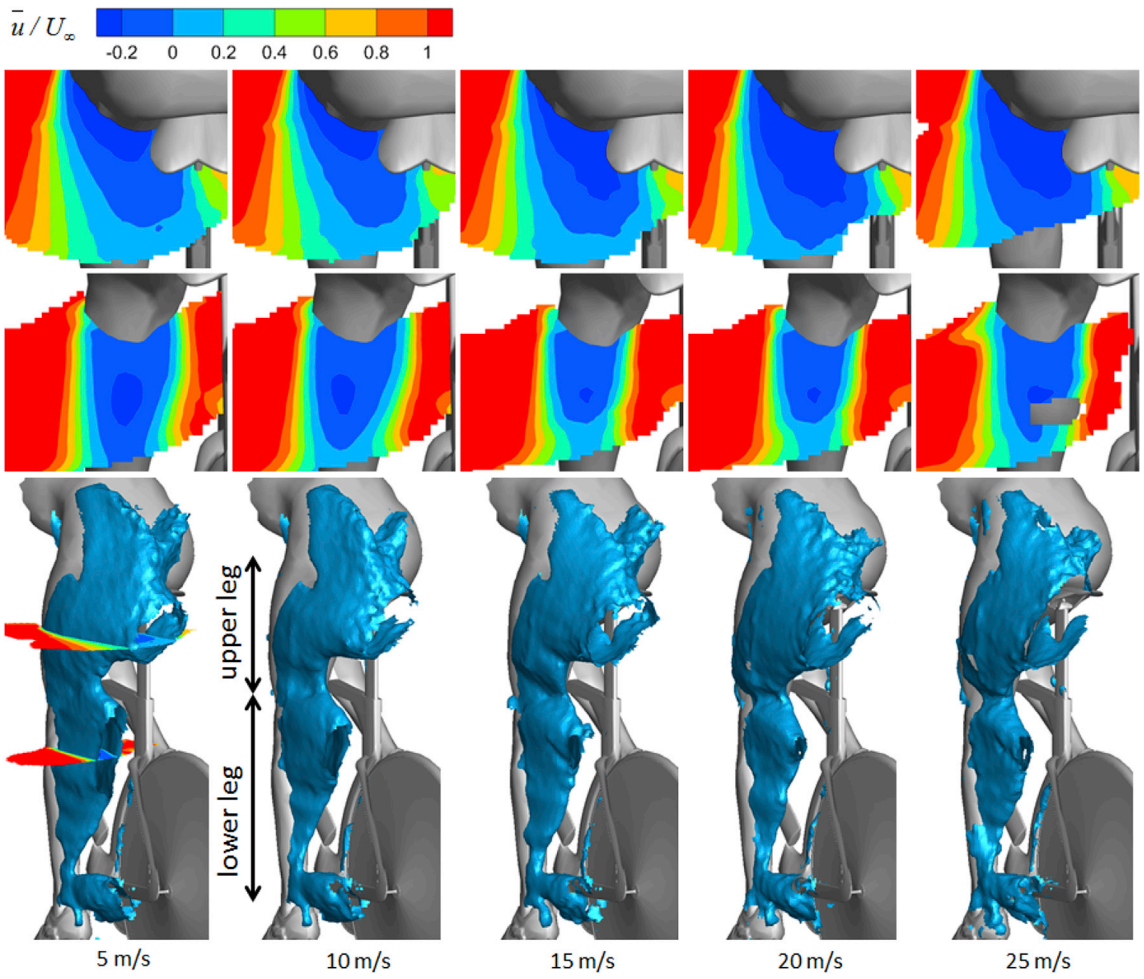

Fig. 8. Contours of non-dimensional streamwise velocity at $y = 950$ mm (top) and $y = 650$ (middle) and iso-surfaces of $\bar{u}/U_\infty = 0.2$ (bottom).

Table 3
Characteristic velocities and dimensions of recirculation region of the flow across the leg at different y-positions.

U_∞ [m/s]	Max reverse velocity [$\bar{u}/U_\infty$]			Reattachment length [L/d]			Wake width [d_w/d]		
	at y-position [mm]			at y-position [mm]			at y-position [mm]		
	425	650	950	425	650	950	425	650	950
5	−0.10	−0.24	−0.27	1.46	~2.2	1.58	0.91	1.14	1.23
10	−0.06	−0.22	−0.27	0.85	2.02	1.59	0.70	1.14	1.20
15	−0.08	−0.21	−0.28	1.23	1.70	1.70	0.74	1.02	1.34
20	−0.08	−0.18	−0.29	0.90	1.70	1.85	0.61	1.00	1.30
25	−0.09	−0.22	−0.29	0.80	1.80	~1.80	0.57	1.00	1.25

In contrast to the lower leg, the wake of the upper leg generally widens and elongates between $U_\infty = 5$ m/s and $U_\infty = 20$ m/s (Fig. 8-bottom). At $y = 950$ mm, the recirculation region clearly grows in size between $U_\infty = 10$ m/s and 20 m/s (Fig. 8-top). The relative increases in reattachment length and peak reverse velocity in the latter range of freestream speed are approximately 10% (Table 3). This particular behaviour is also observed comparing the profiles of streamwise velocity obtained at $x_\zeta/d = 0.8$. The recirculation region is narrow at $U_\infty = 10$ m/s (marked W_{10} in Fig. 9-top row), in contrast to its width at 20 m/s (marked W_{20}). The Reynolds number effects in the wake of the upper leg are opposite to those observed at the lower leg, which suggests a different mechanism is governing its wake behaviour. This mechanism is addressed later in this section.

Among the different velocity profiles, the Reynolds number effects are possibly most pronounced at $y = 425$ mm (Fig. 9-third row). At this location on the leg the minimum wake velocity increases from approximately $\bar{u}/U_\infty = 0$ to 0.6 at $U_\infty = 5$ m/s and 25 m/s, respectively (difference is marked), as a result of the corresponding decrease of the length of the recirculation region (see Table 3). This comparison among the different locations on the leg suggests that the relative reduction of the wake width peaks at $y = 425$ mm.

The non-dimensional wake width, estimated from the spatial gradient of the streamwise velocity profiles, is depicted in Fig. 10-left at various different y-positions along the leg. At $y = 425$ mm d_w/d generally decays over the full speed range (solid red line), comparable to the drop of the drag coefficient of 2D cylinders and spheres between sub-critical and critical conditions. The wake width decreases over 30% between 5 and 25 m/s, exceeding the reduction of d_w/d at any other location on the leg. The critical velocity is determined as the speed at which d_w/d is minimal. At the lower leg, however, a plateau at the higher speeds, indicating the

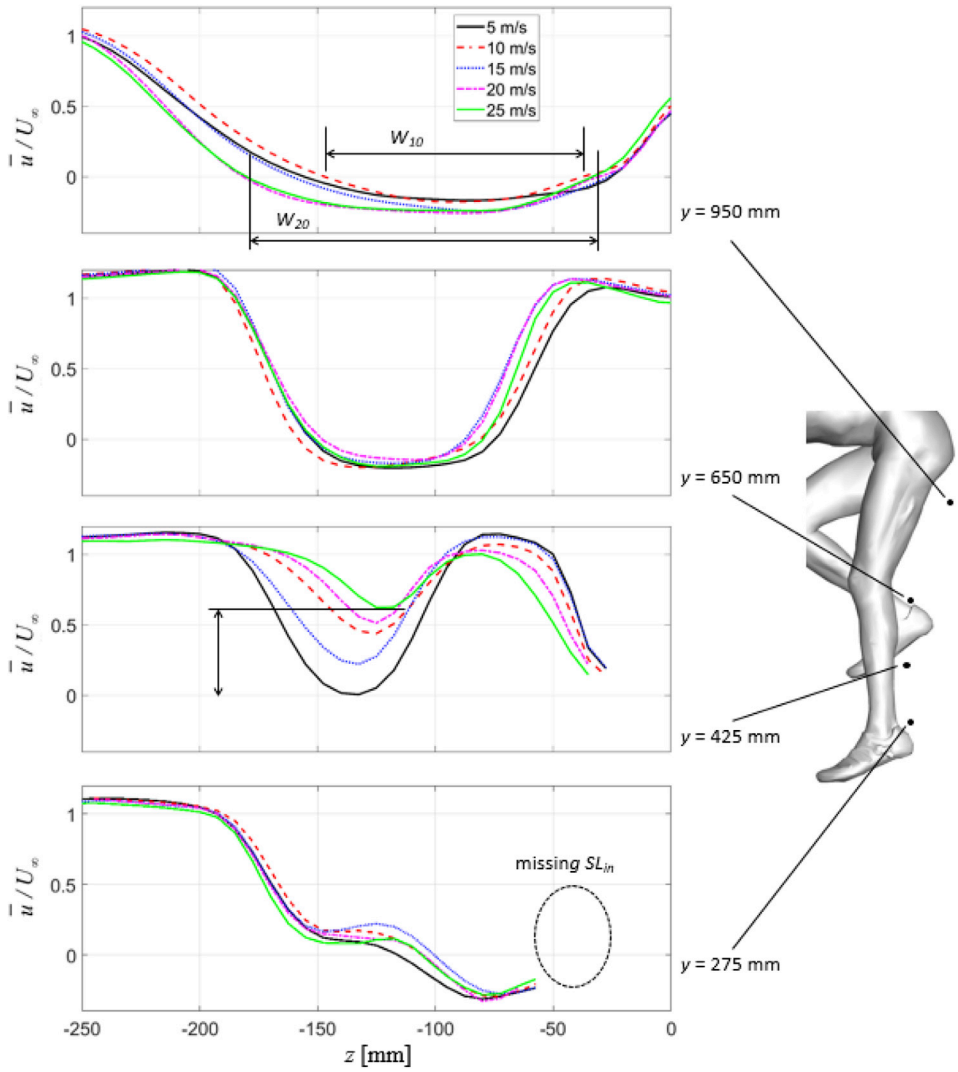

Fig. 9. Spanwise profiles in the near-wake of the leg of non-dimensional time-average streamwise velocity.

proximity of a minimum wake width, is missing; hence, it is concluded that the critical velocity sits beyond the present range of freestream velocity. At the mid-section of the leg, $y = 545$ mm and $y = 650$ mm, a similar drop of the wake width is observed between 5 and 15 m/s. In contrast to the lowest part of the leg, a plateau of relatively constant width is observed at approximately 20–25 m/s (solid black and dashed red lines, respectively). This implies that the critical velocity is within the range of measured speeds and approximately equal to 20–25 m/s.

While the variation of the wake width at the lower leg is largely similar to the isolated 2D cylinder and spherical flow, the observations at the upper leg are different. Between 5 and 10 m/s the upper leg wake width drops, followed by a significant increase between approximately 10 and 20 m/s ($y = 845$ mm and $y = 950$ mm in Fig. 10-left; dash-dot cyan line and dotted blue line, respectively). The former drop is associated with the transition from the sub-critical into the critical regime. The subsequent steep increase cannot be associated to the drag crisis mechanism for an isolated bluff body. It may be ascribed, instead, to the effect of the upstream arm. When the flow across the upper arm transitions from sub-critical to critical, its wake narrows and, hence, the flow upstream of the leg experiences a reduction of velocity deficit. As a consequence, the leg's wake width increases, similar to the increase in drag coefficient of the trailing one of two tandem cylinders (Okajima, 1977). A discussion on the wake width Reynolds number effects of the upper arm is presented in the next section.

4.2.2. *The upper arm*

The wake of the arm features a triangular shape with the apex above the elbow. Downstream of the latter, the streamwise velocity is largely Reynolds number invariant (wake marked in Fig. 11-top-left). This absence of Reynolds number effects is attributed to a turbulent boundary layer that develops over the upstream lower arm. Above the elbow, the wake generally narrows between $U_\infty = 5$ and 25 m/s (marked d_w in Fig. 11-top left and right), although this narrowing is not as significant as for the leg and hip. Close to the trunk-arm junction clear Reynolds number effects in the wake of the arm seem to be absent possibly as a consequence of the proximity of the head (marked in Fig. 11-top-right).

The wake of the head also poses a problem in the identification of the shear layer at the inside of the upper arm. The depicted profiles of streamwise velocity in Fig. 12 highlight a wide profile scatter among the different speeds on the inside of the arm at $y = 1100$ (marked by dashed circle in second row). On the outside of the arm, instead, a significant inward relocation of the outer shear layer is observed (marked ΔSL_{out}). At the trunk-arm junction, where only the outside of the arm is exposed to the air flow, similar Reynolds number effects are observed ($y = 1200$ mm; Fig. 12-top row). At the mid-segment of the upper arm the location of the outer shear layer is rather invariant, while the inner shear layer shifts inwards (marked ΔSL_{in} in Fig. 12-third row). Finally, at the elbow it is observed that the velocity does not decrease below approximately 0.2 with little to no differences at the different speeds. The closely spaced

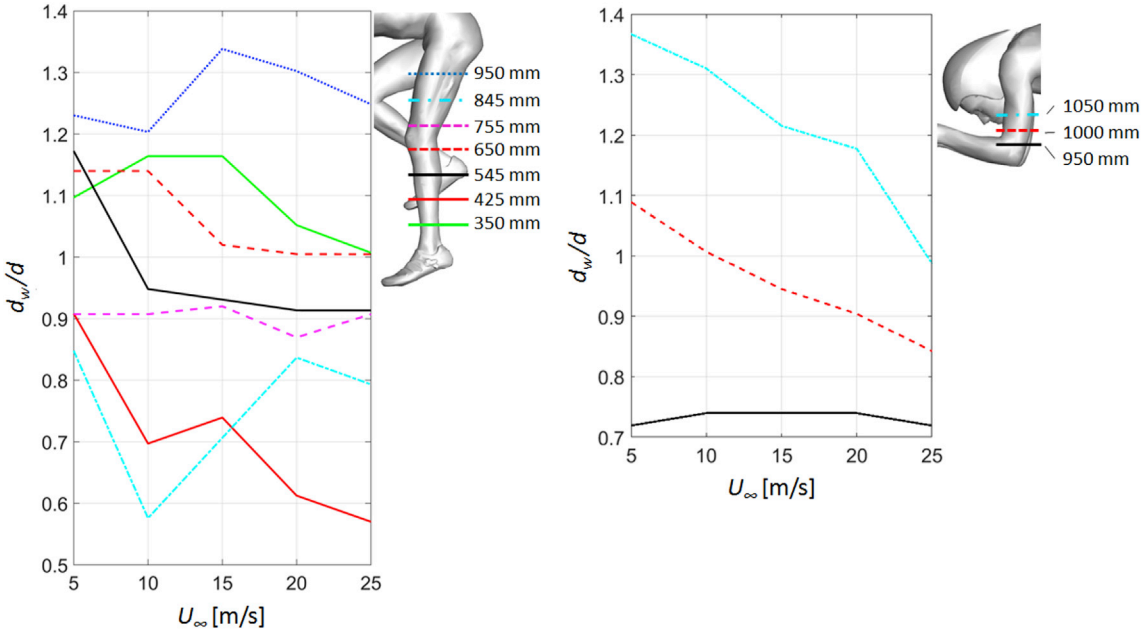

Fig. 10. Non-dimensional wake width at increasing freestream velocity at different height along the leg (left) and the arm (right).

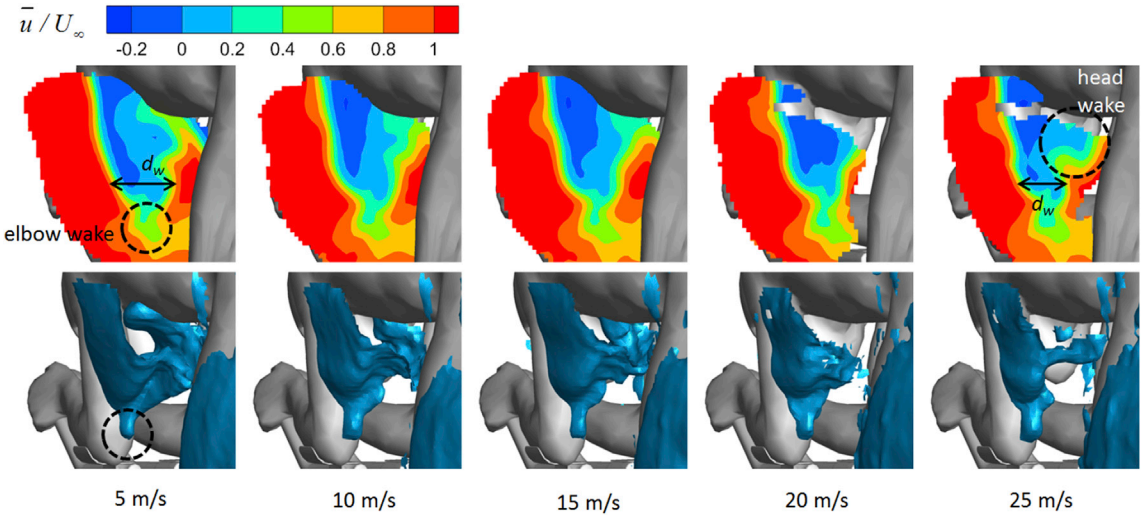

Fig. 11. Contours of non-dimensional streamwise velocity at $x = 240$ mm (top) and iso-surfaces of $\overline{u}/U_\infty = 0.2$ (bottom).

profiles indicate the negligible variation of the elbow wake width, which is depicted in Fig. 10-right (solid black line). The wake width in the mid-segment of the arm, $y = 1000$ and $y = 1050$, monotonically decays over the full range of freestream speeds, similarly to that of the lower leg. Hence, the critical velocity exceeds the maximum freestream velocity considered in this work.

4.2.3. The hip and lower back

In contrast to the arm and leg, the flow across the hip and lower back is strongly three dimensional and the width of its wake cannot be estimated in a similar way as for the previous cases. The discussion of the flow Reynolds number effects is presented more qualitatively. Fig. 13 presents iso-surfaces of $\overline{u}/U_\infty = 0.2$ (first row), contours of non-dimensional streamwise velocity (second row), vertical velocity (third row) and non-dimensional streamwise vorticity (fourth row). Two branches of strong velocity deficit develop asymmetrically over the lower back (marked L and R in the top two Fig. 13-left) as a consequence of the asymmetric leg position. These branches stretch further upstream at low freestream velocity (5 m/s $\leq U_\infty \leq$ 10 m/s) compared to the higher freestream speeds, suggesting a delayed flow separation in the latter conditions. As a consequence the peak downwash over the lower back is increased from approximately $\overline{w}/U_\infty = -0.4$ to $\overline{w}/U_\infty = -0.55$ at 5 m/s $< U_\infty <$ 10 m/s and 15 m/s $< U_\infty <$ 25 m/s, respectively. Another consequence is an increase of the area of reverse flow behind the hip and lower back (indicated in Fig. 13-second row). The delayed separation and increased downwash also introduce an increase of streamwise vorticity ($\overline{\omega}C/U_\infty$ increases from approximately -4.5 to -8.5) from the left thigh vortex (indicated in Fig. 13-middle-bottom). Variations in the right thigh vortex cannot be observed, as it crosses the boundary of the measurement domain. It is concluded that the most significant change in flow topology in the present range of Reynolds numbers occurs between 10 m/s $< U_\infty <$ 15 m/s, as also observed for the upper leg flow.

4.3. Spatial variation of wake width, critical velocity and drag reduction

The wake width is examined along the cyclist's arm and leg every 15

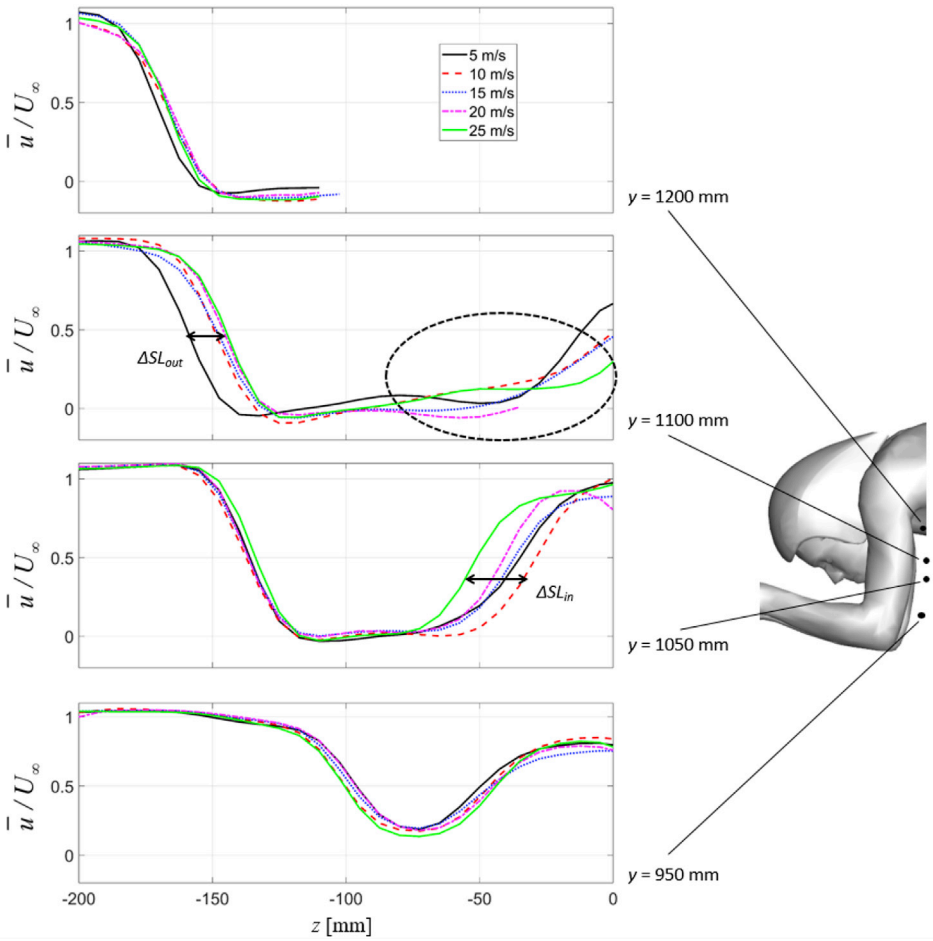

Fig. 12. Spanwise profiles of non-dimensional time-average streamwise velocity in the near-wake of the upper arm.

mm and at each value of the freestream velocity (Fig. 14-left). It is observed that the spatial variation of the width along the leg is similar among the different speeds: minima of d/d_w are observed around $y \sim 400$ mm and $y \sim 850$ mm. This has been ascribed to the streamwise vortex pairs of the shank and upper leg, respectively. Furthermore, the large width at the top of the leg is the consequence of the merged left and right leg wakes. The critical velocity along the leg is depicted in Fig. 14-middle and its uncertainty is indicated by the grey bandwidth. Three different regions can be distinguished: 1) the lower leg (320 mm $< y <$ 500 mm), 2) the knee region (500 mm $< y <$ 780 mm) and 3) the upper leg (780 mm $< y <$ 1000 mm), which have been marked green, orange and purple (Fig. 14-top middle), respectively. In the first region, the flow across the lower leg, the wake width decays rather monotonically over the full range of freestream velocity. Hence, the critical velocity is out of the present range of freestream velocity and exceeds 25 m/s, which is indicated by a right-pointing arrow symbol. In the knee region, the wake width exhibits a major reduction from $U_\infty = 5$ m/s to $U_\infty = 15$ m/s, and then it maintains approximately constant for $U_\infty \geq 15$ m/s, with a minor reduction between 15 m/s and 20 m/s. As a consequence, the critical velocity is estimated around 20 m/s, with an uncertainty typically exceeding 5 m/s. The boundaries of this region, where $V_{crit} \sim 15$ m/s, coincide with the location of the streamwise vortex pairs emanating from the shank and upper leg (see Fig. 8) indicating that the flow Reynolds number effects of the leg are partly governed by these vortex structures. In both the lower leg and knee region, drag reductions may be achieved by tailored application of surface roughness considering a typical race speed $V_{race} = 15$ m/s. This is in contrast to the third region. Along the upper leg the wake width drops significantly between $U_\infty = 5$ m/s and $U_\infty = 10$ m/s, and then increases again for higher free-stream velocities. Hence, the critical velocity is $V_{crit} = 10$ m/s and drag reduction may be achieved further polishing the leg's surface.

The upper arm may be divided into two different regions: The elbow (900 mm $< y <$ 950 mm) and the mid-arm (950 mm $< y <$ 1100 mm), marked red and blue, respectively in Fig. 14-bottom-middle. The flow across the elbow does not exhibit typical drag crisis behaviour and, hence, no critical velocity exists. Conversely, in the mid-arm region the wake width drops significantly with increasing free-stream velocity. Similar to the lower leg, the critical condition is not reached in the present range of free-stream velocities. It is likely that the critical speed exceeds that of the lower leg considering the relatively large discrepancy between the wake width at 20 and 25 m/s in Fig. 14-bottom left.

Finally, the reduction of the local drag coefficient with respect to race speeds, $\Delta C_{D,crit}/C_{D,race}$ is depicted in Fig. 14-right, with $\Delta C_{D,crit} = C_{D,race} - C_{D,crit}$. In here $C_{D,race}$ is the drag coefficient at $V_{race} = 15$ m/s, while $C_{D,crit}$ is obtained through equation (2). This relative drag coefficient reduction should be considered as a qualitative indication of the possible drag reduction among different regions on the cyclist body. It is observed that the most significant drag reductions are possible along the lower leg and the upper arm. A reduction of the critical velocity of the upper arm through application of surface roughness, however, may partly be balanced by an increase of the drag of the upper leg as a consequence of the reduced velocity deficit approaching it. In contrast to the lower leg and upper arm, the possible drag reduction is significantly smaller in the knee region as a consequence of critical velocity being closer to race speed.

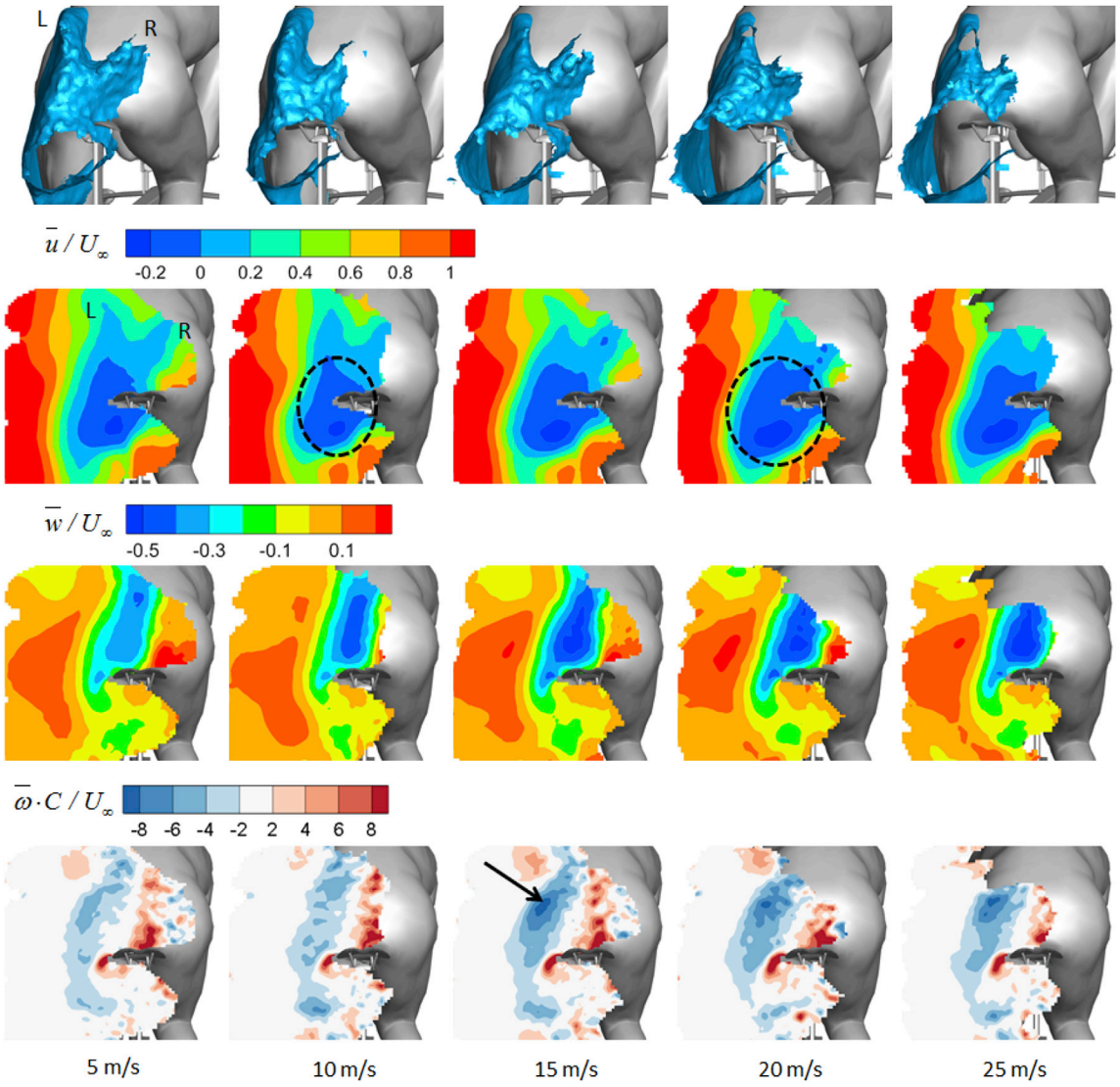

Fig. 13. Iso-surfaces of 0.2 $\bar{u}/U_\infty$(top), contours of non-dimensional streamwise velocity (second row), vertical velocity (third row) and streamwise vorticity (bottom) at $x = 860$ mm.

5. Discussion

In the literature it has been hypothesized that the critical flow condition on leg models occurs at different speeds at different locations, because of its tapered geometry, and, hence, the drag crisis on the entire leg is not observed at one specific Reynolds number (e.g. Brownlie et al., 2009). Considering the results of the present work, that hypothesis is partly true. Indeed, starting from the ankle upwards, the critical velocity generally decays along the lower leg and knee region. In addition, however, other mechanisms affect the critical velocity and Reynolds number effects as well. The critical velocity on the cyclist limbs is governed locally by streamwise counter-rotating vortex pairs, such as the upper leg and shank vortices. Furthermore, wake interactions caused by the upstream arm, lead to Reynolds number effects opposite to those observed at isolated body parts. The Reynolds number effects in the regions that are not affected by these mechanisms are similar to those observed at isolated two-dimensional cylinders, depicting a significant decrease in wake width along the critical flow regime.

The authors realize that an experimental investigation such as that described in the present work is practically infeasible for most organisations that are responsible for the design of low-drag skinsuits, mostly because of the required PIV expertise and equipment. So instead of conducting these measurements for every new skinsuit, the present findings should serve as a reference and can be used in addition to the measurements that are conventionally conducted on isolated cylinders. Although the mannequin employed in the present investigation features specific anthropometric characteristics and is installed in a particular position, the model characteristics that affect the critical velocity can be considered typical features of a time-trial cyclist: legs with a thickness that increase from the ankle up, a knee junction between the upper and the lower leg and the upper arm being upstream of the upper leg. Hence, a general set of guidelines for the design of low-drag skinsuits can be distilled from this investigation. Based on the present finding the local aerodynamic drag along the cyclist's lower leg, knee and upper arm can be reduced by application of surface roughness. To achieve the critical flow condition all along the limbs, the roughness on the upper arm and lower leg should be most pronounced, while in the knee region the roughness should be less articulated. In contrast, the aerodynamic drag of the upper leg may be reduced using extremely smooth fabrics. Note that the above recommendations to add surface roughness in the lower leg and knee region of the cyclist is currently in contradiction with cycling international regulations (uci.org). These regulations, however, describing on which parts of the legs a suit may be worn, may change in the future. Furthermore, the present findings may be used in sports such

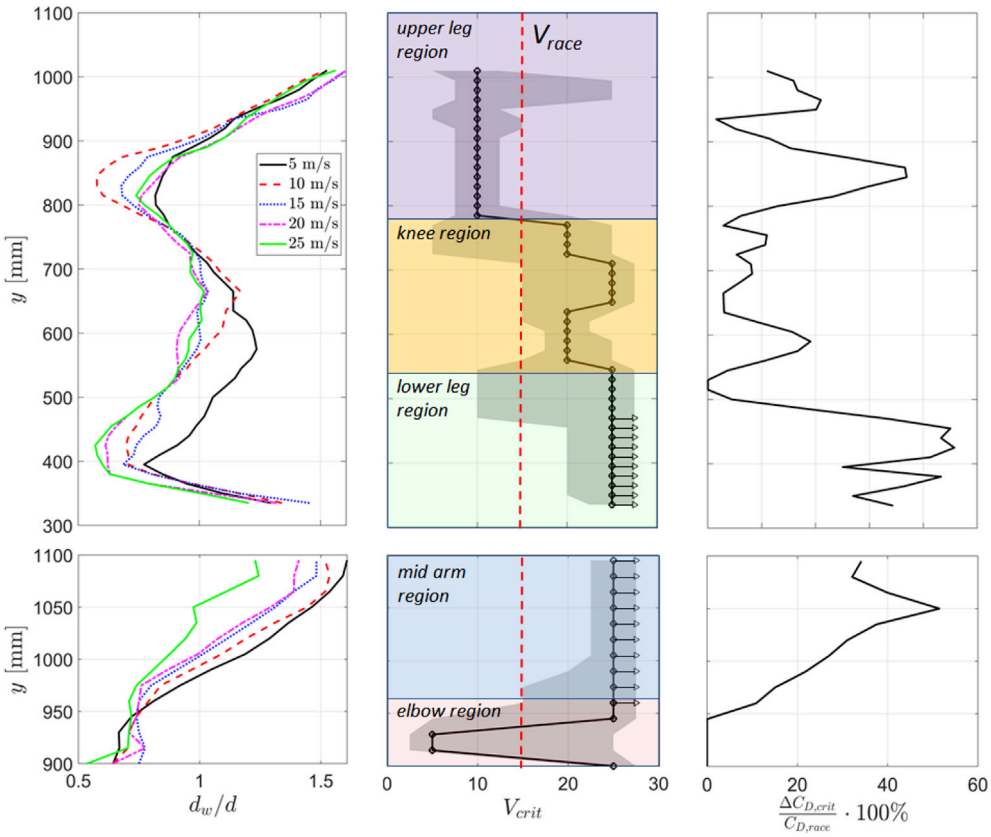

Fig. 14. Wake width at increasing freestream velocity (left), critical velocity (middle) and relative drag coefficient reduction (right) along the leg (top) and the arm (bottom). The critical velocity uncertainty bandwidth is indicated by the shaded area and the red dashed line indicates typical race speed. (For interpretation of the references to colour in this figure legend, the reader is referred to the Web version of this article.)

as speed skating, where such regulations are absent, and athlete position and speed is somehow similar to that in cycling.

An obvious limitation of the present investigation is the focus on the left side of the mannequin, the one with the leg extended. An investigation to the right side of the cyclist may confirm the assumptions of the authors that the Reynolds number effects in the wake of the flexed leg are much weaker as a consequence of 1) the more streamwise oriented upper and lower leg and 2) the larger knee angle and the corresponding increase of the strength of the counter rotating streamwise vortices emanating from the upper leg and shank (Jux et al., 2018). Furthermore, extending the present investigation to different crank angles would complement the understanding of the near-wake Reynolds number effects and the distribution of critical velocity. In addition, an investigation on a pedaling cyclist model may provide further insights. The pedaling motion induces additional streamwise and vertical velocity components to the leg and, hence, changes the orientation and magnitude of the leg's approach flow, thus likely affecting the critical velocity. For such a study, first the uncertainty of the present critical velocity estimation (2.5 m/s) should be reduced in order to measure the effect of these additional velocity components which remain generally below 2 m/s (crank length of 0.17 m and pedaling frequency of 1.7 Hz).

Apart from the above limitations of the experimental measurements, it should be noted that in practice a cyclist likely experiences conditions that are different from those seen during the present wind tunnel measurements. In particular the freestream turbulence may be different and the cyclist is at non-zero yaw angle as a consequence of cross-winds. It is well known that the former, the flow turbulence, affects the laminar to turbulent boundary layer transition, flow separation and, hence, the critical Reynolds number (e.g. D'Auteuil et al., 2012). A detailed flow turbulence characterization of a cyclist in race conditions, however, is missing in literature and, hence, the present turbulence conditions cannot be compared to assess the possible effect on the critical flow condition. Finally, note that the present work has been conducted at zero yaw angle. In practice, in the presence of cross-wind, the cyclist Reynolds number effects may differ from the present findings, for example, as a result of the interaction of the wake of the front wheel and the leg. Hence, in future work the present work may be repeated in a range of different yaw angles.

6. Conclusions

The flow downstream of a cyclist mannequin's left arm, leg and hip is investigated using robotic volumetric Particle Image Velocimetry at freestream velocities of [5 10 15 20 25] m/s. The near wake of these limbs features typical bluff body characteristics: two shear layers bounding a region of reverse flow. The width and length of the recirculation region increase with increasing body segment thickness. Moreover, this reverse flow area is governed by multiple streamwise counter-rotating vortex pairs that strongly reduce its size locally. The wake width of the lower leg and arm reduces with increasing freestream velocity. This variation is related to a variation in drag coefficient and depicts typical drag crisis behaviour as that encountered for isolated cylinders. In contrast, an increase in wake width is observed on the upper leg, which is attributed to the corresponding decrease of the upstream arm's wake width. A distribution of the so-called *critical velocity*, the freestream speed at which the wake width is minimal, allows dividing the leg into different regions. 1) The lower leg region features a critical velocity that exceeds 25 m/s, the maximum of the present range of speeds; 2) The critical velocity in the knee region is approximately 20–25 m/s and 3) the upper leg critical velocity equals 10 m/s. Similar to the lower leg, also along the upper arm the critical velocity exceeds 25 m/s. Furthermore, it is concluded that critical flow condition is not only governed by the taper of

the cyclist limbs. Instead, streamwise counter-rotating vortex pairs and limb wake interactions should also be considered in future cycling skinsuit design to achieve critical flow conditions along each body segment, and consequently have minimum aerodynamic drag at race speed.

Declaration of competing interest

The authors declare that they have no known competing financial interests or personal relationships that could have appeared to influence the work reported in this paper.

CRediT authorship contribution statement

W. Terra: Writing - review & editing. **A. Sciacchitano:** Supervision. **F. Scarano:** Supervision.

Acknowledgements

Francesco Scarano is acknowledged for his work during the experiments. Constantin Jux is acknowledged for allowing the use of his data in the present work (Jux et al., 2018).

References

Achenbach, E., 1968. Distribution of local pressure and skin friction around a circular cylinder in cross-flow up to $Re = 5 \times 10^6$. J. Fluid Mech. 34 (4), 625–639.
Achenbach, E., 1971. Influence of surface roughness on the cross flow around a cylinder. J. Fluid Mech. 46 (2), 321–335.
Achenbach, E., 1972. Experiments on the flow past spheres at very high Reynolds numbers. J. Fluid Mech. 54 (3), 565–575.
Achenbach, E., Heinecke, E., 1981. On vortex shedding from smooth and rough cylinders in the range of Reynolds numbers 6×10^3 to 5×10^6. J. Fluid Mech. 109, 239–251.
Adrian, R.J., 1997. Dynamic ranges of velocity and spatial resolution of particle image velocimetry. Meas. Sci. Technol. 8, 1393–1398.
Agüera, N., Cafiero, G., Astarita, T., Discetti, S., 2016. Ensemble 3D PTV for high resolution turbulent statistics. Meas. Sci. Technol. 27, 124011.
Barry, N., Burton, D., Sheridan, J., Thompson, M., Brown, N.A.T., 2015. Aerodynamic drag interactions between cyclists in team pursuit. Sports Eng. 18, 93–103.
Blocken, B., Druenen, T. van, Topolar, Y., Malizia, F., Mannion, P., Andrianne, T., Marchal, T., Maas, G., Diepens, J., 2018b. Aerodynamic drag in cycling pelotons: new insights by CFD simulation and wind tunnel testing. J. Wind Eng. Ind. Aerod. 179, 319–337.
Blocken, B., Topolar, Y., Andrianne, T., 2016. Aerodynamic benefit for a cyclist by a following motorcycle. J. Wind Eng. Ind. Aerod. 155, 1–10.
Blocken, B., van Druenen, T., Toparlar, Y., Andrianne, T., 2018a. Aerodynamic analysis of different cyclist hill descent positions. J. Wind Eng. Ind. Aerod. 181, 27–45.
Brownlie, L., Kyle, C., Carbo, J., Demarest, N., Harber, E., MacDonald, R., Nordstrom, M., 2009. Streamlining the time trial apparel of cyclists: the Nike Swift Spin project. Sports Technol. 2, 53–60.
Caridi, G.C.A., Ragni, D., Sciacchitano, A., Scarano, F., 2016. HFSB-seeding for large-scale tomographic PIV in wind tunnels. Exp. Fluid 57, 190.
Chabroux, V., Mba, M.N., Sainton, P., Favier, D., 2010. Wake characteristics of time trial helmets using PIV-3C technique. In: Proceedings of the 15th Int Symp on Applications of Laser Techniques to Fluid Mechanics (Lisbon, Portugal).
Constantinescu, G., Squires, K., 2004. Numerical investigations of flow over a sphere in the subcritical and supercritical regimes. Phys. Fluids 16, 1449.
Crouch, T.N., Burton, D., Brown, N.A.T., Thomson, M.C., Sheridan, J., 2014. Flow topology in the wake of a cyclist and its effect on aerodynamic drag. J. Fluid Mech. 748, 5–35.
Crouch, T.N., Burton, D., Thompson, M.C., Brown, N.A.T., Sheridan, J., 2016. Dynamic leg-motion and its effect on the aerodynamic performance of cyclists. J. Fluid Struct. 65, 121–137.
D'Auteuil, A., Larose, G.L., Zan, S.J., 2012. Wind turbulence in speed skating: measurement, simulation and its effect on aerodynamic drag. J. Wind Eng. Ind. Aerod. 104–106, 585–593.
Defraeye, T., Blocken, B., Koninckx, E., Hespel, P., Carmeliet, J., 2010. Aerodynamic study of different cyclist positions: CFD analysis and full-scale wind-tunnel tests. J. Biomech. 43 (7), 1262–1268.
Defraeye, T., Blocken, B., Koninckx, E., Hespel, P., Carmeliet, J., 2011. Computational fluid dynamic analysis of drag and convective heat transfer of individual body segments for different cyclist positions. J. Biomech. 44, 1695–1701.
Giaquinta, D., 2018. The Flow Topology of the Ahmed Body in Cross-Wind. MSc Thesis. Delft University of Technology, Department of Aerospace Engineering.
Griffith, M.D., Crouch, T., Thompson, M.C., Burton, D., Sheridan, J., Brown, N.A., 2014. Computational fluid dynamics study of the effect of leg position on cyclist aerodynamic drag. J. Fluid Eng. 136 (10), 101105.
Jux, C., Sciacchitano, A., Schneiders, J.F.G., Scarano, F., 2018. Robotic volumetric PIV of a full-scale cyclist. Exp. Fluid 59, 74.
Kawamura, T., Hiwada, M., Hibino, T., Mabushi, I., Kumada, M., 1984. Flow around a finite circular cylinder on a flat plate. Bulletin of JSME 27, 232, 10.
Lehmkuhl, O., Rodriguez, I., Borell, R., Chiva, J., Oliva, A., 2014. Unsteady forces on a circular cylinder at critical Reynolds numbers. Phys. Fluids 26, 125110.
Lignarolo, L.E.M., Ragni, D., Krishnaswami, C., Chen, Q., Simão Ferreira, C.J., Van Bussel, G.J.W., 2014. Experimental analysis of the wake of a horizontal-axis wind-turbine model. Renew. Energy 70, 31–46.
Lukes, R.A., Hart, J.H., Chin, S.B., Haake, S.J., 2005. The understanding and development of cycling aerodynamics. Sports Eng. 8, 59–74.
Norberg, C., 1983. Interaction between freestream turbulence and vortex shedding for a single tube in cross-flow. J. Wind Eng. Ind. Aerod. 23, 501–514.
Oggiano, L., 2010. Drag reduction and aerodynamic performances in Olympic sports. Dr. theses NTNU 118, 2010.
Oggiano, L., Troynikov, O., Konopov, I., Subic, A., Alam, F., 2009. Aerodynamic behaviour of single Jersey fabrics with different roughness and cover factors. Sports Eng. 12, 1_12.
Okajima, A., 1977. Aerodynamic characteristics of stationary tandem cylinders at high Reynolds numbers. Bull. Jpn. Soc. Mech. Eng. 22, 504–511.
Park, C.W., Lee, S.J., 2000. Free end effects on the near wake flow structure behind a finite circular culinder. J. Wind Eng. Ind. Aerod. 88, 231–246.
Rodriguez, I., Lehmkuhl, O., Chiva, J., Oliva, A., 2015. On the flow past a circular cylinder from critical to super-critical Reynolds numbers: wake topology and vortex shedding. Int. J. Heat Fluid Flow 55, 91–103.
Roshko, A., 1955. On the wake and drag of bluff bodies. J. Aeronaut. Sci. 22, 124–132.
Roshko, A., 1961. Experiments on the flow past a circular cylinder at very high Reynolds number. J. Fluid Mech. 10, 345–356.
Saredi, E., Sciacchitano, A., Scarano, F., 2019. Multi-Δt 3D-PTV based on Reynolds decomposition. In: Proceedings 13th Int Symp on PIV (Munich).
Scarano, F., Ghaemi, S., Caridi, G.C.A., Bosbach, J., Dierksheide, U., Sciacchitano, A., 2015. On the use of helium-filled soap bubbles for large-scale tomographic PIV in wind tunnel experiments. Exp. Fluid 56, 42.
Schanz, D., Gesemann, S., Schroeder, A., 2016. Shake the Box: Lagrangian particle tracking at high particle image densities. Exp. Fluid 57–70.
Schewe, G., 1983. On the force fluctuations acting on a circular cylinder in crossflow from subcritical up to transcritical Reynolds numbers. J. Fluid Mech. 133, 265–285.
Schneiders, J.F.G., Jux, C., Sciacchitano, A., Scarano, F., 2018. Coaxial volumetric velocimetry. Meas. Sci. Technol. 29, 065201.
Sciacchitano, A., Scarano, F., 2014. Elimination of PIV light reflections via a temporal high pass filter. Meas. Sci. Technol. 25 (8), 084009.
Terra, W, Sciacchitano, A, Scarano, F, 2019. Aerodynamic drag determination of a full-scale cyclist mannequin from large-scale PTV measurements. Exp Fluids 60 (29). https://doi.org/10.1007/s00348-019-2677-6.
Unnikrishnan, S., Gaitonde, D.V., 2019. First-mode-induced nonlinear breakdown in a hypersonic boundary layer. Comput. Fluids 191. https://doi.org/10.1016/j.compfluid.2019.104249, 104249.
Van Tubergen, J., Verlinden, J., Stroober, M., Baldewsing, R., 2017. Suited for performance: fast full-scale replication of athlete with FDM. In: Proceedings of SCF'17. Cambridge, MA, USA, June 12–13 2017.
White, B.L., Nepf, H.M., 2008. A vortex-based model of velocity and shear stress in a partially vegetated shallow channel. Water Resour. Res. 44 https://doi.org/10.1029/2006WR005651. W01412.
Zdravkovich, M.M., 1987. The effects of interference between circular cylinders in cross flow. J. Fluid Struct. 1, 239–261.
Union cycliste internationale. https://www.uci.org/inside-uci/constitutions-regulations/equipment, 2019.